

AEROSOL CONSTRAINTS ON THE ATMOSPHERE OF THE HOT SATURN-MASS PLANET WASP-49 b

PATRICIO E. CUBILLOS,¹ LUCA FOSSATI,¹ NIKOLAI V. ERKAEV,² MATEJ MALIK,³ TETSUYA TOKANO,⁴ MONIKA LENDL,^{1,5}
COLIN P. JOHNSTONE,⁶ HELMUT LAMMER,¹ AND AURÉLIEN WYTENBACH⁷

¹Space Research Institute, Austrian Academy of Sciences, Schmiedlstrasse 6, A-8042, Graz, Austria

²Federal Research Center "Krasnoyarsk Science Center" SB RAS, "Institute of Computational Modelling", Krasnoyarsk 660036, Russia

³Center for Space and Habitability, University of Bern, Sidlerstrasse 5, CH-3012, Bern, Switzerland

⁴Institut für Geophysik und Meteorologie, Universität zu Köln, Albertus-Magnus-Platz, 50923 Köln, Germany

⁵Max Planck Institute for Astronomy, Königstuhl 17, 69117 Heidelberg, Germany

⁶Department of Astrophysics, University of Vienna, Türkenschanzstrasse 17, 1180 Vienna, Austria

⁷Geneva Observatory, University of Geneva, ch. de Maillettes 51, CH-1290 Versoix, Switzerland

ABSTRACT

The strong, nearly wavelength-independent absorption cross section of aerosols produces featureless exoplanet transmission spectra, limiting our ability to characterize their atmospheres. Here we show that even in the presence of featureless spectra, we can still characterize certain atmospheric properties. Specifically, we constrain the upper and lower pressure boundaries of aerosol layers, and present plausible composition candidates. We study the case of the bloated Saturn-mass planet WASP-49 b, where near-infrared observations reveal a flat transmission spectrum between 0.7 and 1.0 μm . First, we use a hydrodynamic upper-atmosphere code to estimate the pressure reached by the ionizing stellar high-energy photons at 10^{-8} bar, setting the upper pressure boundary where aerosols could exist. Then, we combine HELIOS and Pyrat Bay radiative-transfer models to constrain the temperature and photospheric pressure of atmospheric aerosols, in a Bayesian framework. For WASP-49 b, we constrain the transmission photosphere (hence, the aerosol deck boundaries) to pressures above 10^{-5} bar ($100\times$ solar metallicity), 10^{-4} bar (solar), and 10^{-3} bar ($0.1\times$ solar) as lower boundary, and below 10^{-7} bar as upper boundary. Lastly, we compare condensation curves of aerosol compounds with the planet's pressure-temperature profile to identify plausible condensates responsible for the absorption. Under these circumstances, we find as candidates: Na_2S (at $100\times$ solar metallicity); Cr and MnS (at solar and $0.1\times$ solar); and forsterite, enstatite, and alabandite (at $0.1\times$ solar).

Key words: planets and satellites: atmospheres – planets and satellites: individual: WASP-49 b – methods: numerical – techniques: spectroscopic

1. INTRODUCTION

Over the past decade, photometric observations of transiting exoplanets have become the main tool to characterize exoplanet atmospheres. Transit or eclipse events provide a direct measurement of the transmission or emission spectrum of a planetary atmosphere, respectively. The temperature and composition of an atmosphere modulate an observed spectrum, as each atmospheric species has a very specific spectral absorption pattern. Therefore, multi-wavelength observations allow us to disentangle the contribution of different species, constraining atmospheric properties.

Unfortunately, characterizing atmospheres has been proven to be a more challenging effort than expected, since many exoplanet observations show nearly featureless spectra (e.g., Pont et al. 2008, Mandell et al. 2013, Knutson et al. 2014, Kreidberg et al. 2014a). Muted spectral features are attributed to the presence of cloud condensates and photochemical hazes (hereafter, aerosols), whose strong opacities and weak wavelength dependence obscure other spectral

features from deeper regions of an atmosphere. In light of the ubiquity of aerosol features in exoplanet atmospheres, researchers have adopted two different approaches, either study the prominence of cloud-covered atmospheres to avoid selecting these targets, or better characterize atmospheric aerosol properties.

The current sample of well-studied exoplanet atmospheres (good spectral coverage and data quality) is just enough to enable tentative trends in the cloud prominence. Stevenson (2016) found a higher cloud prominence for the more temperate (equilibrium temperature $T_{\text{eq}} < 700$ K) and lower surface gravity planets ($\log g < 2.8$), based on the strength of the 1.4 μm H_2O band. Heng (2016) found a tentative lower cloudiness index for the more irradiated atmospheres, based on the alkali absorption line profiles. Lastly, Barstow et al. (2017) found evidence of aerosol absorption in all 10 planets from Sing et al. (2016). Overall, finding that planets with $1300 \text{ K} < T_{\text{eq}} < 1700 \text{ K}$, are more consistent with gray cloud layers, whereas other planets are more consistent with strong Rayleigh scattering absorption.

Although the lack of features of aerosols makes them intrinsically hard to characterize, several studies have improved our understanding of their properties and consequences on exoplanet atmospheres and spectra. For example, Wakeford & Sing (2015) studied the effects of grain sizes and distributions on hot-Jupiter transmission spectra, finding absorption features which could differentiate condensate formation scenarios, such as condensate clouds or photochemically generated species. Morley *et al.* (2015) determined variations in the optical albedo between cloudy (moderate) and hazy (dark) atmospheres for warm planets, or thermal inversions caused by hazes. Parmentier *et al.* (2016) have studied how variations in the cloud composition with equilibrium temperature shape the transmission spectrum of hot Jupiter atmospheres. These and other theoretical studies help us to provide more accurate diagnostics when we encounter cloud-dominated observations.

In this article we further explore on the characterization of cloudy atmospheres, investigating what properties can we constrain given present-day ground-based transmission spectra. We study the case of the bloated Saturn-mass but Jupiter-sized planet WASP-49 b, which presents a flat near-infrared (NIR) transmission spectrum. By applying a mixed forward and retrieval-modeling approach, we characterize the atmosphere of WASP-49 b with a combination of hydrodynamic, radiative-transfer, and equilibrium-condensation atmospheric models. Assuming that the observations are the result of an optically thick aerosol layer, we constrain the pressure boundaries of the layer, and then list plausible aerosol condensates for different atmospheric metallicity scenarios. In Section 2, we summarize the properties and observations of the WASP-49 system. In Section 3, we model the atmosphere of WASP-49 b. Finally, in Section 4 we present our conclusions.

2. WASP-49 b TRANSMISSION SPECTRUM

The hot Jupiter-sized exoplanet WASP-49 b (Lendl *et al.* 2012) has a mass of $M_p = 0.40 \pm 0.03 M_{\text{Jup}}$, radius $R_p = 1.2 \pm 0.05 R_{\text{Jup}}$, and equilibrium temperature $T_{\text{eq}} = 1400 \pm 40$ K (assuming negligible Bond albedo). Lendl *et al.* (2016) reported multiple NIR broad-band transmission observations with the FORS2 instrument of the ESO/VLT, from 0.7 μm to 1.0 μm . These observations revealed a nearly flat, featureless optical spectrum (Figure 1). The lack of spectral features in the transmission spectra suggests that the atmosphere of WASP-49 b has an optically thick cloud deck, blocking the atomic and molecular features.

For a clear atmosphere, the NIR spectrum is particularly useful to constrain the atmospheric composition, as there are strong and isolated molecular and atomic features. Atmospheric sodium and potassium produce strong, broad, and localized absorption lines (centered at 0.59 and 0.77 μm , respectively). H_2O is the most abundant molecule spectroscopically active in this range. At solar abundances, H_2O produces a clear absorption band at 0.9–1.0 μm . If present, TiO and VO dominate most of this region of the spectrum. However, the heavy TiO and VO molecules can easily con-

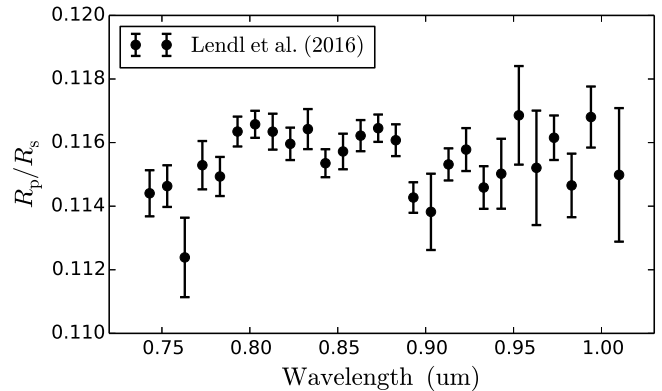


Figure 1. WASP-49 b FORS2 transmission spectrum from Lendl *et al.* (2016). For a clear atmosphere, K and H_2O absorption features should increase the modulation spectrum at 0.78 μm and 0.95 μm , respectively.

dense and rain out toward higher pressures for temperatures lower than ~ 1500 K (Fortney *et al.* 2008, Spiegel *et al.* 2009). We do not expect to find TiO and VO in the atmosphere of WASP-49 b at the altitude sampled by the FORS2 observations.

3. ATMOSPHERIC MODELING

To constrain the aerosol properties of WASP-49 b, we model the planetary atmosphere with a succession of models. First, we study the upper atmosphere of the planet with hydrodynamic models to determine the depth of the stellar high-energy irradiation, constraining the upper boundary of the aerosol layer. Then, we use radiative-transfer models to retrieve the pressure corresponding to the transit radius of the planet (the photospheric pressure). This is the range of pressures where the aerosols condensate, making the atmosphere optically thick. Finally, we use the constraint on the aerosol pressure boundaries to propose plausible condensate species responsible for the flat transmission spectra, by comparing the planet temperature profile to condensation curves of known condensates.

3.1. Hydrodynamic Modeling

The stellar incident high-energy irradiation drives the planetary upper-atmosphere chemistry and dynamics. In particular, stellar X-ray and extreme-ultraviolet (XUV) photons deposit large amounts of energy into the atmosphere, raising the temperature and dissociating atmospheric molecules. The effective XUV radius (where most of the stellar XUV flux is deposited) sets the upper boundary where aerosols can exist.

To study the upper atmosphere of WASP-49 b, we apply the 1D hydrodynamic model of Erkaev *et al.* (2016). This model solves the mass, momentum, and energy-conservation system of equations, allowing us to derive the pressure, temperature, and composition profiles of WASP-49 b, fully considering the stellar XUV irradiation, Ly- α cooling, and atmospheric ionization, dissociation, and recombination. This model considers a simplified hydrogen chemistry, and thus we consider the result from this model only for upper layers

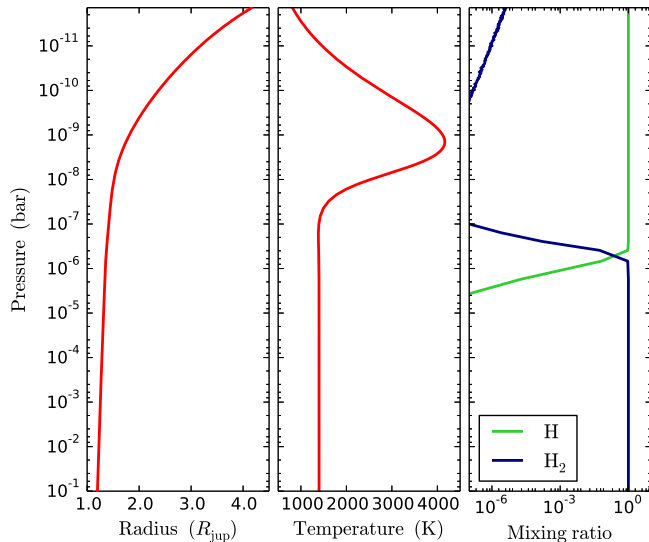


Figure 2. WASP-49b atmospheric profile derived from the hydrodynamic model. The left, middle, and right panels show the radius, temperature, and composition profiles for WASP-49b as function of pressure.

of an atmosphere, where most of the atmospheric particles are dissociated (Koskinen et al. 2013).

We estimate the XUV luminosities for WASP-49 b using the scaling laws of Wright et al. (2011) to convert the stellar rotation rates and masses into X-ray luminosities, and Sanz-Forcada et al. (2011) to convert the X-ray luminosities into extreme-ultraviolet luminosities. At the orbit of the planet, we obtain X-ray and extreme-ultraviolet fluxes of $240 \text{ erg s}^{-1} \text{ cm}^{-2}$ and $2500 \text{ erg s}^{-1} \text{ cm}^{-2}$, respectively.

Figure 2 shows the output atmospheric profiles from the hydrodynamic model for WASP-49 b. The abrupt increase in temperature at $\sim 10^{-8}$ bar reveals where most of the stellar high-energy irradiation is being deposited, and therefore, marks the XUV effective radius. Hydrogen dissociates at slightly higher pressures, between 10^{-6} bar and 10^{-7} bar. The extremely high temperatures reached at the XUV effective radius (~ 4000 K) are sufficient to evaporate any atmospheric condensate. Therefore, we set the 10^{-8} bar level as the uppermost boundary where aerosol condensates can remain. The XUV effective radius remains approximately at the same pressure when we change the stellar irradiation fluxes by an order of magnitude.

We estimate the particle falling timescales to investigate its role in determining the presence of cloud particles at these low pressures. The falling timescale of particles is $\tau_f = H/v_t$, where H is the pressure scale height and v_t is the terminal velocity of particles. The terminal velocity for each condensed species can be calculated (e.g., Spiegel et al. 2009) as

$$v_t = \frac{2}{9} \frac{a^2 \rho_c g}{\eta}, \quad (1)$$

where a is the particle radius, ρ_c is the mass density of the condensate, g is the gravitational acceleration and η is the dynamic viscosity of air.

The mass density of the condensates considered in this study lies in the range between 1170 kg m^{-3} (for NH_4SH) and 7874 kg m^{-3} (for Fe). The gravitational acceleration of WASP-49b amounts to 7.18 m s^{-2} with the estimated mass and radius of this planet. The dynamic viscosity of gaseous H_2 at 1000 K is 0.019 Pa s according to the gas viscosity calculator¹. The scale height of an H_2 atmosphere at 1000 K with the above g amounts to $5.75 \times 10^5 \text{ m}$.

These numbers yield v_t of $9.8\text{--}66.1 \times 10^{-8} \text{ m s}^{-1}$ for a $1 \mu\text{m}$ -sized cloud particle and $9.8\text{--}66.1 \times 10^{-4} \text{ m s}^{-1}$ for a $100 \mu\text{m}$ -sized particle. Consequently, the falling timescale is $0.9\text{--}5.9 \times 10^{12} \text{ s}$ for $1 \mu\text{m}$ and $0.9\text{--}5.9 \times 10^8 \text{ s}$ for $100 \mu\text{m}$. Thus, the resulting terminal velocities are small, as is typical for cloud particles.

3.2. Radiative-transfer Modeling

The flat broad-band transmission spectrum of WASP-49 b not only suggests that the planet has an aerosol layer, it also constrains the altitude where the atmosphere becomes opaque, i.e., the photosphere. However, the corresponding photospheric pressure remains a degenerate parameter that depends on the atmospheric temperature, composition, and aerosol opacity. Here, we combine forward and retrieval radiative-transfer models to constrain the photospheric pressure of WASP-49 b.

3.2.1. Radiative-equilibrium Temperature Model

To get a first idea of the atmospheric state of WASP-49 b, we compute radiative-equilibrium atmospheric models using the HELIOS radiative-transfer code (Malik et al. 2017). The goal is to obtain representative atmospheric temperature values by running ad-hoc simulations with and without aerosol layers. The radiative-transfer runs consider infrared and shorter-wavelength opacities from H_2O , CO_2 , and CO (Rothman et al. 2010); CH_4 , NH_3 , HCN , and C_2H_2 (Rothman et al. 2013); H_2S (Azzam et al. 2016); the alkali metals Na and K (Heng et al. 2015, Heng 2016); collision-induced absorption from $\text{H}_2\text{-H}_2$ and $\text{H}_2\text{-He}$ (Richard et al. 2012); and H_2 Rayleigh scattering.

The atmospheric model consists of a one-dimensional log-spaced-pressure model, extending from 10^3 bar to 10^{-9} bar. We compute radiative-equilibrium temperature profiles subject to an emission brightness temperature of 1400 K, i.e., the equilibrium temperature WASP-49 b. The atmosphere receives an incident stellar irradiation modeled with a PHOENIX spectrum, according to the parameters of Lendl et al. (2016). We keep a fixed solar-metallicity composition in thermochemical equilibrium (Stock et al. 2017, in prep.). The chemistry model includes around 550 gas-phase species and is based on the semi-analytic approach described in Gail & Sedlmayr (2013).

To simulate an aerosol layer, we include a log-normally distributed gray-opacity absorber over pressure. We set the standard deviation of the distribution to 1.0 in $\log_{10}(\text{pressure})$ and test two altitudes for the peak, 10^{-5} bar and 10^{-6} bar.

¹ <https://www.lmnoeng.com/Flow/GasViscosity.php>

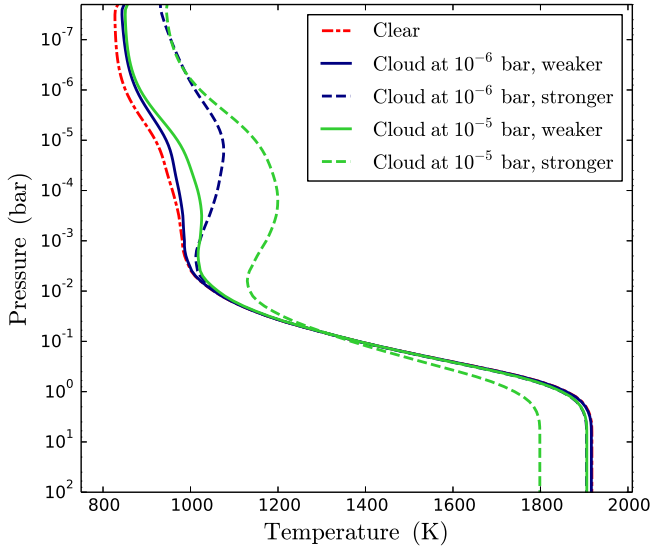


Figure 3. HELIOS radiative-equilibrium temperature profiles for WASP-49 b. The models are constrained such that the total output flux corresponds to a brightness temperature of 1400 K. All models consider the main opacity sources relevant for Jupiter-like exoplanets. The cloud models consist of a log-normally distributed opacity in pressure with total opacity $k = 10^{-2} \text{ cm}^2 \text{ g}^{-1}$ (weaker) and $10^{-1} \text{ cm}^2 \text{ g}^{-1}$ (stronger, see legend).

We also model two cases for the total aerosol opacity of $k = 10^{-2} \text{ cm}^2 \text{ g}^{-1}$ and $10^{-1} \text{ cm}^2 \text{ g}^{-1}$. These clouds have non-isotropic scattering and a non-vanishing albedo. We estimated these parameters from MgSiO_3 aerosol particles with size $\sim 5 \mu\text{m}$, using a Mie-scattering code. Since we do not know the cloud composition, this condensate provides a good first-order guess for silicate albedos. The obtained albedos range on the order of a few percent, with the lower clouds the maximum albedo, up to $A \approx 0.17$. As silicate clouds are mostly forward scattering (asymmetry parameter $g_0 \sim 0.7-0.9$), their absorption effect outweighs their reflective effect of stellar radiation. Thus, the net effect of the clouds causes a global warming of atmospheric temperatures.

Figure 3 shows the radiative-equilibrium temperature profiles for WASP-49 b. The greenhouse gasses, namely H_2O , CO_2 , and CH_4 , dominate the absorption at depth (and thus, the heating). The aerosol layer produces a weak-to-moderate temperature increase with respect to the clear-atmosphere model. The peak of the heating is located a few scale heights below the aerosol layer, and is proportional to the aerosol opacity, as expected. The Na and K resonance doublet lines dominate the absorption at the highest layers of the atmosphere (above $\sim 10^{-7}-10^{-8}$ bar). However, at these high altitudes, the atmosphere is already directly interacting with the high-energy stellar irradiation, where the radiative-equilibrium assumptions (i.e., hydrostatic and thermo-chemical equilibrium) do not hold anymore. Thus, we trust the radiative-equilibrium profiles up to the $\sim 10^{-8}$ bar level. Between pressures of 0.1 and 10^{-8} bar (the region probed by NIR transmission spectroscopy), the atmospheric temperature ranges between 800 K and 1200 K.

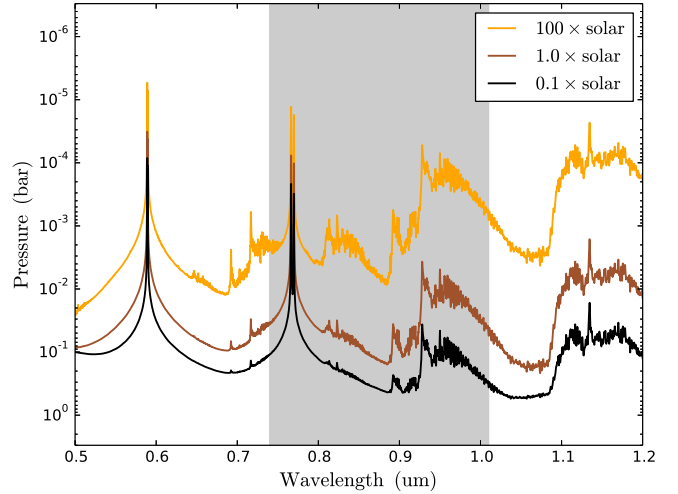


Figure 4. WASP-49 b clear-atmosphere model transmission spectra. This is the pressure corresponding to the transit radius modulation. The different models have scaled solar metallicities (see legend), with abundances in thermochemical equilibrium at the planet’s equilibrium temperature (1400 K). The shaded area denotes the wavelength range probed by the FORS2 transmission observations. Aerosol layers would need to sit above these pressures to hide these spectral features.

3.2.2. Transmission Photospheric-Pressure Retrieval

The observed NIR transmission spectrum of WASP-49 b (Fig. 1) constrains the transit radius of the planet. However, this dataset does not directly constrain the pressure (p_T) at the transit radius. Assuming that the flat NIR spectrum of WASP-49 b is the result of an opaque aerosol layer, upon additional considerations, we can obtain posterior distributions for p_T , and hence, the cloud top level. An opaque aerosol layer must lay high enough in the atmosphere to blanket other spectral features remain unobserved; in this case, the H_2O band at $0.95 \mu\text{m}$, the K doublet at $0.77 \mu\text{m}$, and the Rayleigh H_2 slope (Figure 4). Finding this pressure is a degenerate problem that hinges also on the unconstrained atmospheric temperature and composition, beside the aerosol properties themselves.

Everything considered, we adopt a Bayesian retrieval approach to constrain the transmission photospheric pressure of the planet. To this end, we model the NIR transmission spectrum of WASP-49 b with the Python Radiative-transfer in a Bayesian framework package (Pyrat Bay, Cubillos *et al.*, in prep.). Pyrat Bay is a state-of-the-art, open-source, reproducible package², which is an update of the Bayesian Atmospheric Radiative Transfer package (Cubillos 2016, Blecic 2016). To explore the parameter space, Pyrat Bay implements the differential-evolution Markov-chain Monte Carlo (MCMC) algorithm (Cubillos *et al.* 2017b).

The planet’s atmospheric model consist of a one-dimensional set of spherically concentric shells (layers), equidistantly spaced in log pressure. We considered 100 layers ranging from 10^{-8} bar to 100 bar. For transmission geometry, Pyrat Bay computes the fraction of absorbed stellar flux for parallel

² <https://github.com/pcubillos/pyratbay>.

rays (along the star–planet–Earth line of sight) crossing the planetary atmosphere.

To explore different composition scenarios, we test three cases with 0.1, 1.0, and 100 times enhanced solar elemental metallicities. For each case we compute thermochemical-equilibrium abundances (Blecic et al. 2016), which we keep fixed during the MCMC exploration. Our atmospheric models include all major species expected in gas-giant planets (H_2O , CO_2 , CO , CH_4 mainly). However, only H_2O and K produce strong enough absorption features in the observed spectral range. We compute the H_2O line-transition opacity from the HITEMP database (Rothman et al. 2010). We also include collision-induced absorption opacities for H_2 – H_2 (Borysow 2002, Borysow et al. 2001) and H_2 –He (Borysow et al. 1988, 1989, Borysow & Frommhold 1989); resonant Na and K lines (Burrows et al. 2000); and Rayleigh scattering opacity (Lecavelier Des Etangs et al. 2008). We do not expect to find TiO in the atmosphere since TiO condenses around 2000–1400 K for pressures between 1 bar and 10^{-8} bar (Spiegel et al. 2009).

There is a large variety of candidate aerosol condensates. Each one forms and remains in the atmosphere at specific pressure and temperature conditions, but overall, covering a broad range of the parameter space (e.g., Wakeford & Sing 2015). Unfortunately, when considering a limited wavelength region, most condensates produce similar, nearly featureless spectra, making it hard to spectroscopically distinguish one from another. Thus, it is impractical to determine the specific condensates in a retrieval. Instead, we model and fit a generic semi-infinite gray absorber with constant opacity cross-section.

Given the penetration depth of the stellar high-energy flux estimated by our upper-atmosphere hydrodynamic models (Section 3.1), we set the aerosol top-boundary pressure at 10^{-8} bar. We leave the aerosol opacity cross-section ($f_{\text{gray}} \times \sigma_0$) as an MCMC free parameter, with $\sigma_0 = 5.3 \times 10^{-27} \text{ cm}^2 \text{ molec}^{-1}$ (the H_2 opacity cross-section at 0.7 μm) and f_{gray} a dimensionless scaling factor. The aerosol extinction coefficient (in cm^{-1}) at each layer results from multiplying the cross-section with the H_2 number density. Therefore, the aerosol extinction coefficient scales linearly with pressure. Note that we use the H_2 just as reference values for the parameters.

We assume hydrostatic equilibrium to relate the pressure and radius of the atmospheric layers. To obtain the particular solution to the hydrostatic-equilibrium differential equation we need to include a ‘boundary’ condition $p(r_0) = p_0$, where p is the atmospheric pressure and p_0 the pressure at the radius r_0 . Here, we fix p_0 at 0.1 bar, and leave $r_0 \equiv R_{0.1 \text{ bar}}$ as an MCMC free parameter. The p_0 and r_0 pair is implicitly constrained by the transmission spectrum, although it typically degenerates with other atmospheric parameters.

The unknown temperature profile influences the output transmission spectrum by modifying both the line-transition opacity of the species and the hydrostatic-equilibrium solution. The degeneracy with other atmospheric properties renders the temperature mostly unconstrained by the MCMC,

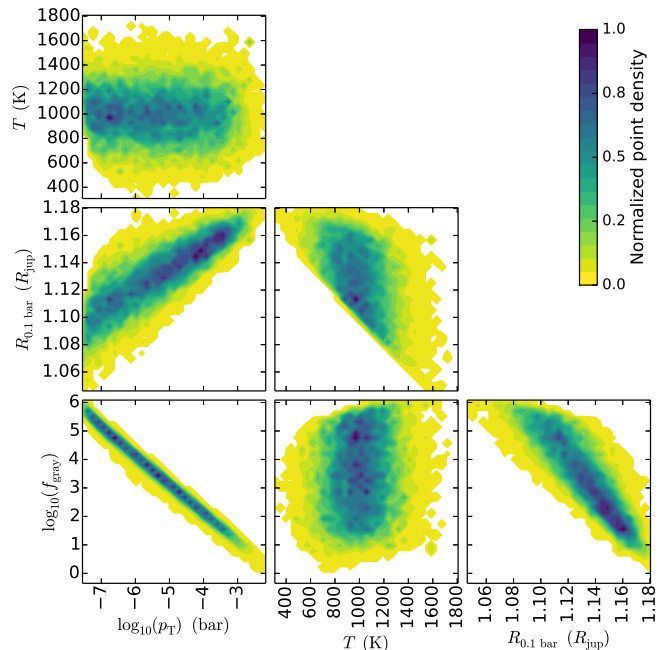


Figure 5. MCMC pairwise posterior distribution for the solar-abundance run. Note that only T , $R_{0.1 \text{ bar}}$, and f_{gray} are the MCMC free parameters, the photospheric pressure p_T is a derived parameter (see text).

given our limited transmission data. Thus, our model adopts a simple isothermal profile, with the temperature T an MCMC free parameter. This is an appropriate model, considering that the radiative-equilibrium models show temperature profiles that do not dramatically change above 0.1 bar—the temperature at deeper layers are irrelevant since those pressures are not accessible by the transmission observation (see Fig. 4). We further limit the temperature range explored by the MCMC by including a Gaussian prior centered at 1200 K and with standard deviation of 200 K. This range covers the temperatures sampled by the radiative-equilibrium models. This prior effectively prevents the MCMC to sample extremely low temperatures which, however physically plausible, are unlikely. Later, the posterior distributions will show that this prior does not influence the conclusions of this work.

3.2.3. WASP-49 b Retrieval Results

For WASP-49 b, we ran an MCMC for each of the three composition scenarios, with T , $R_{0.1 \text{ bar}}$, and $\log(f_{\text{gray}})$ the retrieval MCMC free parameters. Figure 5 shows the pairwise MCMC posterior distributions for the solar-abundance run. The runs for 0.1 and 100 times solar metallicity are qualitatively similar. Additionally, knowing the pressure and radius profile for each iteration, we derive the pressure corresponding to the observed transit radius, $p_T = p(R_p)$. As seen in Figure 5, the main factor that determines p_T is the aerosol opacity, and thus, this transit pressure effectively constrains the top of the aerosol layer.

The correlation between free parameters in the posteriors reflects the degeneracy of the fit. Among these parameters, the temperature is the least constrained by the data. Conse-

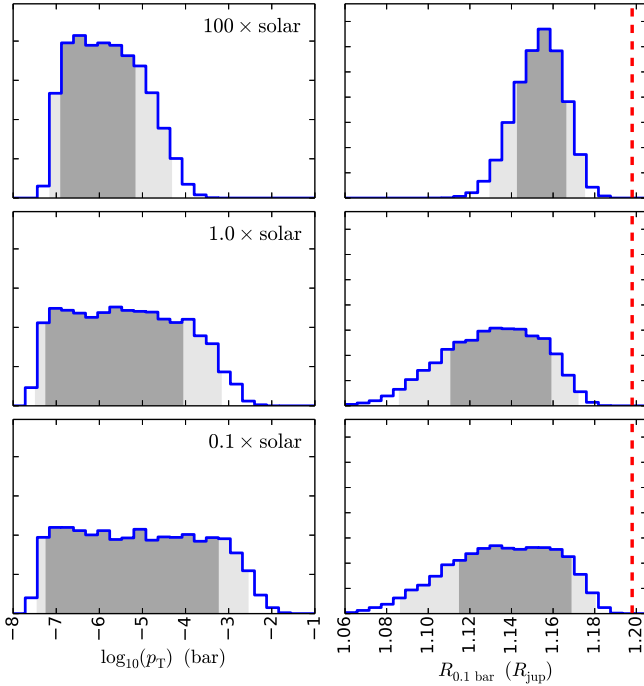


Figure 6. Marginal posterior density of p_T and $R_{0.1 \text{ bar}}$ vs. metallicity. The histograms are plotted to scale such that the area under the curve is one. The light and dark gray areas denote the 95% and 68% highest-posterior-density (HPD) credible regions, respectively. The red dashed vertical line denotes the NIR transit radius of WASP-49 b, observed by FORS2.

quently, the marginal posterior distribution for the temperature replicates the adopted prior distribution. Although the arbitrariness in the temperature prior selection expresses in the MCMC posteriors, this has a minor effect on the photospheric pressure. While there are correlations between p_T and $R_{0.1 \text{ bar}}$ and $\log(f_{\text{gray}})$, there is weak to no correlation between p_T and T .

Figure 6 shows the MCMC marginal posterior distributions for p_T and $R_{0.1 \text{ bar}}$, for each of the composition case. Depending on the atmospheric metallicity, the atmospheric-retrieval runs indicate that an aerosol layer should locate between $\sim 10^{-7}$ bar (at the top) and $\sim 10^{-3}$ bar to $\sim 10^{-5}$ bar (at the bottom) to explain the flat transmission spectrum (68% highest-posterior-density, HPD).

The atmospheric metallicity plays an important role in constraining the transmission photospheric pressure. Given that the spectral features arise at lower pressures for a higher-metallicity atmosphere (Fig. 4), and that the aerosols have to make the atmosphere optically thick at even lower pressures (such that the model fit the flat transmission data), the high-pressure boundary of p_T is located at lower pressures for higher metallicities. Furthermore, having no further observational constraints, the lower-pressure boundary of p_T is set by the XUV effective radius at 10^{-8} bar (Section 3.1).

3.3. Equilibrium-clouds Modeling

Now that we have constrained the pressure range where aerosols make the atmosphere optically thick, we investigate which compounds can be responsible for the flat trans-

mission spectrum by comparing the atmospheric temperature and pressure against equilibrium condensation curves.

Our analysis is based on thermochemical equilibrium calculations that are dominant at temperatures higher than 1000 K (Visscher *et al.* 2006, 2010, Morley *et al.* 2012). We assume that the atmosphere can contain an unspecified number of mineral molecules in chemical equilibrium with these atmospheric profiles. Assuming elemental abundances in the solar system (Lodders 2003), thermochemical equilibrium determines the abundance of each species (partial pressure) in equilibrium with a given temperature. The partial pressure can then be put into relation with the temperature-dependent saturation vapor pressure of each species. Once the partial pressure of the species is determined, it can be converted to the equilibrium condensation temperature, which can readily be compared to the atmospheric temperature. The equilibrium condensation temperature generally increases with increasing total pressure and metallicity. Deviations from thermochemical equilibrium can arise due to photochemical reactions in the upper atmosphere or strong convective mixing, but they are neglected in this approach.

Figure 7 depicts the equilibrium condensation temperature profiles of 12 species for the three metallicities tested (100, 1.0, and 0.1 times solar) of the atmosphere, calculated after Visscher *et al.* (2006, 2010) and Morley *et al.* (2012) depending on the species. The equilibrium condensation temperature is the temperature below which a given species can exist in condensed form under a given pressure.

Having no observational temperature constrain (e.g., from a secondary-eclipse observation), we consider HELIOS radiative-equilibrium temperature models for each metallicity and with a cloud layer centered at 10^{-6} bar and opacity of $k = 10^{-1} \text{ cm}^2 \text{ g}^{-1}$. Varying the abundances has important effects on the infrared cooling/heating of the atmosphere. The higher abundance of greenhouse gasses in the 100 \times solar model produces substantially warmer temperatures at depth. However, by definition, the net effective atmospheric temperature remains the same, as the photosphere is simply pushed upward to cooler layers. Additionally, the cloud effect becomes diminished relative to the increased gaseous opacity, as the latter increases with higher metallicity (note that this is a direct outcome of the modeling choice, as the aerosol opacity is constant for each opacity). If strong short-wave absorbers like TiO, VO, or a dark photochemical haze were able to remain high in the atmosphere, the increase in metallicity may lead to a temperature inversion.

Given an atmospheric temperature profile, we can constrain which condensates are consistent with the aerosol layer for each metallicity. Fig. 7 shows that at 100 times solar metallicity, sodium sulfide (Na_2S) is the most plausible condensate in the atmosphere of WASP-49 b. As we explore lower metallicities, the condensation curves shift toward lower temperatures, and thus we expect alabandite (MnS) and Cr to intersect the temperature profile at the pressures where we expect the aerosol layer. For sub-solar metallicities forsterite (Mg_2SiO_4), enstatite (MgSiO_3), Fe, Cr, and alabandite are expected to condense at the required pres-

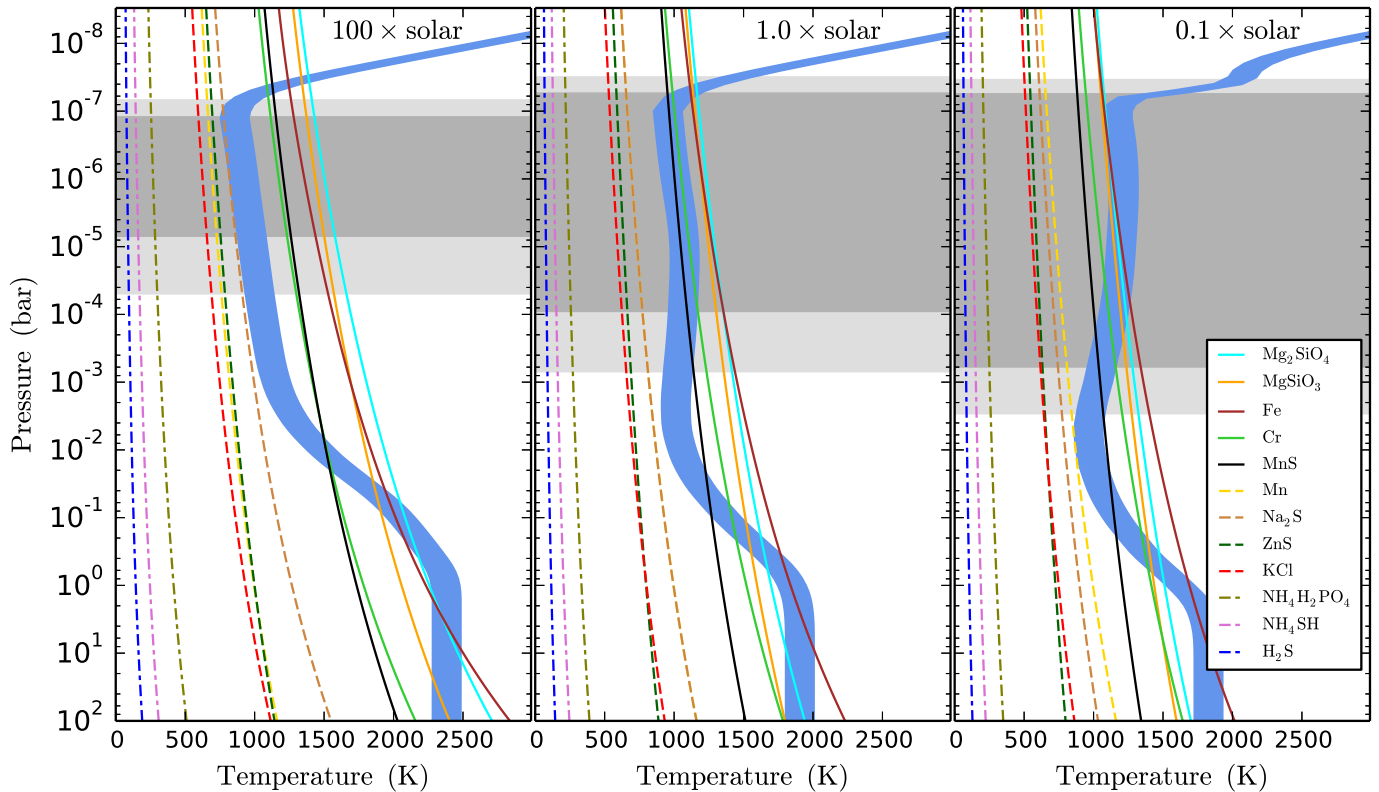


Figure 7. Equilibrium condensation curves for a set of minerals as a function of pressure (see legend). Each of the three panels corresponds to an atmospheric metallicity case. The light and dark gray areas denote the 95% and 68% HPD credible regions (respectively) of the photospheric pressure (Section 3.2.2). The blue band is the radiative-equilibrium temperature profile (Section 3.2.1) for the cloudy case at 10^{-6} bar with stronger opacity. The top of the temperature profile follows the XUV irradiation heat-up curve determined from the hydrodynamic models. The temperature-profile curve has a width of 200 K to consider a range of possible temperatures.

tures. However, we note that, in general, gas-giant planets are not expected to have sub-solar metallicities (Kreidberg et al. 2014b).

A caveat for this scenario is that some the condensates may rain out of the upper atmospheres due to a “cold trap” phenomenon. Since the temperature profiles cross some of the condensation curves at more than one altitude (particularly the solar and sub-solar cases), the condensed species are expected to be confined at the deeper condensation point, (Hubeny et al. 2003, Fortney et al. 2008). This would deplete the upper atmosphere from the condensates, necessary to create the flat transmission spectra. Spiegel et al. (2009) invokes vigorous turbulent mixing on a macroscopic scale as a way to stir condensates up into lower-pressure layers, even in the presence of a cold trap.

3.4. High-resolution Observations

Recently, Wyttenbach et al. (2017) published HARPS high-resolution transmission observations of WASP-49 b. They reported a spectrally resolved detection of strong Na I D lines, arising from hot (~ 3000 K) high-altitude layers ($\sim 1.5 R_p$) of the atmosphere, located above the layers studied in the previous sections. We decided not to include this dataset into our retrieval analysis, because the high-resolution data requires a different data reduction and modeling than that of the low-resolution data, beyond the scope of this manuscript.

Essentially, ground-based high-resolution data analysis require a double normalization approach where, in addition to the normalization by the out-of-transit spectra, one needs to perform a spectral normalization to remove (or reduce) time-correlated noise introduced by telluric variations (see section 4.1 of Wyttenbach et al. 2017). As a first look at this problem, we present a forward-model approach for the simplified case of isolated absorption lines arising above a wavelength-independent cloud deck. The Pyrat-Bay forward model returns the modulation spectrum:

$$M(\lambda) = \frac{f_{\text{out}}(\lambda) - f_{\text{in}}(\lambda)}{f_{\text{out}}(\lambda)}, \quad (2)$$

where $f_{\text{in}}(\lambda)$ and $f_{\text{out}}(\lambda)$ are the in- and out-of-transit flux spectrum, respectively. Then, $1 - M$ corresponds to $f_{\text{in}}(\lambda)/f_{\text{out}}(\lambda)$. If the continuum is dominated by a gray absorber, we can choose any wavelength λ_{ref} for the spectral normalization, as long as the modulation spectrum at λ_{ref} is dominated by the gray opacity. Then we can compute,

$$\tilde{R} = \frac{1 - M(\lambda)}{1 - M(\lambda_{\text{ref}})} = \frac{f_{\text{in}}(\lambda)/f_{\text{in}}(\lambda_{\text{ref}})}{f_{\text{out}}(\lambda)/f_{\text{out}}(\lambda_{\text{ref}})}. \quad (3)$$

Equation (3) effectively mimics the in- and out-of-transit spectrum ratio in the planet rest frame, $\tilde{\mathfrak{R}}$ (equation 5 of Wyttenbach et al. 2017). Figure 8 (left panel) shows the reduced HARPS high-resolution data from (Wyttenbach et al.

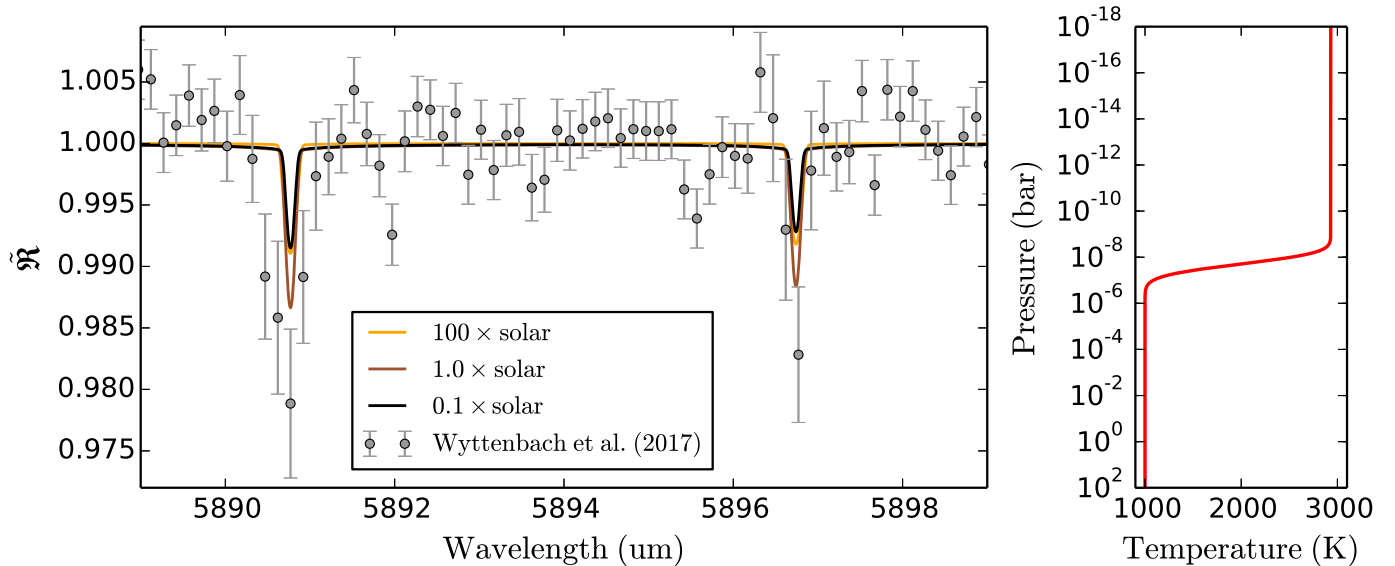


Figure 8. **Left:** WASP-49 b high-resolution transmission spectra. The gray dots with 1σ error bar denote the reduced data from Wyttenbach et al. (2017), binned by 15 points. The solid curves denote our model spectra for each metallicity (see legend), adjusted to the reported spectral resolution of the data. **Right:** atmospheric temperature profile adopted to compute the transmission models.

2017), along with a selected \tilde{R} model for each of our sampled metallicities. Like in the previous section, these models are in thermochemical and hydrostatic equilibrium, but consider an extended hot upper atmosphere at ~ 3000 K (Fig. 8, right panel).

Our models agree with Wyttenbach et al. (2017), that the Na signal is unexpectedly large. Given the lower Na abundance of the sub-solar case, and the smaller scale height of the super-solar case, the solar-abundance case produces the largest Na signal, though in each case our model underestimates the observed signal. To match the observed strength of the Na signal, we would need an enhanced Na abundance, with respect to the other species. Alternatively, at such heights the atmosphere could not necessarily be in local thermodynamic equilibrium. Additionally, for any given metallicity, the Na signal increases with a deeper aerosol layer, suggesting that the cloud deck is located towards the lower end of the found posterior distribution.

With respect to the line width, even with an atmosphere at 3000 K, our models underestimate the width of the Na signal (note that at these altitudes, Doppler broadening dominates the line width). This would suggest that there are strong equatorial winds on the planet (e.g., Louden & Wheatley 2015). In any case, we regard these conclusions as tentative, since to obtain more conclusive constraints from the high-resolution data require a more detailed analysis, and possibly with a more elaborated Sodium absorption profile model.

4. CONCLUSIONS

The presence of cloud condensates or photochemical hazes in the atmosphere of exoplanets limits our ability to characterize these atmospheres. Aerosols not only hide molecular or atomic spectral features from deeper layers in an atmosphere, but also pose a challenge in distinguishing the compounds. This study of WASP-49 b shows that by combining

a number of atmospheric models, we can still constrain atmospheric properties of cloud-covered planets, subject to the observational limitations of current facilities.

Using hydrodynamic atmospheric models we estimate the penetration depth of the stellar high-energy irradiation, located at $\sim 10^{-8}$ bar for WASP-49 b (Fig. 2). This value determines the lowest possible pressure where aerosols could exist, as the high temperatures evaporate the aerosol condensates and high-energy stellar photons can also dissociate the condensates.

Since we do not know the shape of the temperature profile for WASP-49 b, we estimate it from radiative-transfer forward-model runs in radiative equilibrium. From a series of clear and cloudy radiative-equilibrium models, we found that this planet should have temperatures in the 800–1200 K range, above the 0.1 bar level (Fig. 3). Deeper layers are not relevant as they are not accessible by transmission spectra, even in the most favorable case (low-metallicity clear-atmosphere case, Fig. 4).

Then, we retrieve the transmission photospheric pressure of the planet p_T (that corresponding to the transit radius) with an MCMC radiative-transfer run, constrained by the flat NIR transmission spectrum of WASP-49 b. Modeling the aerosol layer as a gray, constant-cross-section absorber we derive the marginal posterior distribution of p_T for three metallicity scenarios, 100, 1.0, and 0.1 times solar elemental abundances, in thermochemical equilibrium. The 68% HPD credible region of p_T is restricted between $\sim 10^{-3}$ – 10^{-5} bar and the $\sim 10^{-7}$ bar levels (Fig. 6). Increasing the metallicity constrains p_T to the smaller region because the aerosol layer needs to blanket the H₂O and K features, which arise from higher layers in the atmosphere. The upper boundary of p_T at $\sim 10^{-7}$ bar is ultimately determined by the penetration depth of the high-energy stellar XUV flux.

Finally, considering that different aerosol compounds condense at different pressures and temperatures, we investigate which are the plausible condensates for each metallicity scenario. Adopting a temperature profile from the radiative-equilibrium models ($\sim 800\text{--}1000$ K), we find a range candidates from sodium sulfide (high metallicity, lower temperature), to alabandite or Cr (solar and low metallicity), to Fe, forsterite, or enstatite (low metallicity).

There are a couple of considerations that could lead to stronger constraints than those found here. Planets with stronger stellar high-energy fluxes should have deeper penetration depths, limiting the upper aerosol boundary. The vibrational mode of small sub-micron sized condensates produce absorption features in the infrared, which could help discern different cloud types, particles sizes, and altitudes (Wakeford & Sing 2015). Clearly, constraining cloudy-atmospheres' properties is heavily limited by both the current data quality and the physical properties of condensates, this exercise is no exception. However, by adopting a number of reasonable assumptions and combining multiple atmospheric models, we showed that one can constrain the location of an aerosol layer on cloudy exoplanets with current data. As more and better-quality data becomes available, these and other theoretical studies will help us to better characterize exoplanet atmospheres, even in the case of cloudy skies.

We thank Dr. Kevin Heng for constructive discussions. We thank contributors to Numpy (van der Walt et al. 2011), SciPy (Jones et al. 2001), Matplotlib (Hunter 2007), the Python Programming Language, and the free and open-source community; the developers of the aastex latex template (AAS Journals Team & Hendrickson 2016); the NASA Astrophysics Data System; and the JPL Solar System Dynamics group for software and services. We thank the anonymous referee for comments that improved the quality the paper. We acknowledge the Austrian Forschungsförderungsgesellschaft FFG projects “RASEN” P847963 and “TAPAS4CHEOPS” P853993, the Austrian Science Fund (FWF) NFN projects S11607-N16 and S11604-N16, and the FWF project P27256-N27. Part of this work has been carried out within the frame of the National Centre for Competence in Research “PlanetS” supported by the Swiss National Science Foundation (SNSF). A.W. acknowledge financial support of the SNSF, grants 200020_152721 and 200020_166227. This article is based on photometric observations made with FORS2 on the ESO VLT/UT1 (Prog. ID 090.C-0758), and the ESO 3.6 m telescope at the La Silla Observatory (ESO Prog. 096.C-0331). The Pyrat-Bay Reproducible Research Compendium (RRC) of this article will be available at https://github.com/pcubillos/CubillosEtal2017_WASP49b once the Pyrat-Bay code gets released for public use.

Software: Pyrat Bay: Python Radiative Transfer in a Bayesian framework (<http://pcubillos.github.io/pyratbay>), HELIOS (<https://github.com/exoclimate/HELIOS>) and latex template (<https://github.com/pcubillos/ApJtemplate>).

REFERENCES

- AAS Journals Team, & Hendrickson, A. 2016, AASJournals/AAS \TeX 6: Version 6.1
- Azzam, A. A. A., Tennyson, J., Yurchenko, S. N., & Naumenko, O. V. 2016, MNRAS, 460, 4063, [ADS, 1607.00499](#)
- Barstow, J. K., Aigrain, S., Irwin, P. G. J., & Sing, D. K. 2017, ApJ, 834, 50, [ADS, 1610.01841](#)
- Blecic, J. 2016, ArXiv e-prints, [ADS, 1604.02692](#)
- Blecic, J., Harrington, J., & Bowman, M. O. 2016, ApJS, 225, 4, [ADS, 1505.06392](#)
- Borysow, A. 2002, A&A, 390, 779, [ADS](#)
- Borysow, A., & Frommhold, L. 1989, ApJ, 341, 549, [ADS](#)
- Borysow, A., Frommhold, L., & Moraldi, M. 1989, ApJ, 336, 495, [ADS](#)
- Borysow, A., Jorgensen, U. G., & Fu, Y. 2001, JQSRT, 68, 235, [ADS](#)
- Borysow, J., Frommhold, L., & Birnbaum, G. 1988, ApJ, 326, 509, [ADS](#)
- Burrows, A., Marley, M. S., & Sharp, C. M. 2000, ApJ, 531, 438, [ADS, astro-ph/9908078](#)
- Cubillos, P., Blecic, J., & Harrington, J. 2017a, in prep.
- Cubillos, P., Harrington, J., Loredó, T. J., Lust, N. B., Blecic, J., & Stemm, M. 2017b, AJ, 153, 3, [ADS, 1610.01336](#)
- Cubillos, P. E. 2016, ArXiv e-prints, [ADS, 1604.01320](#)
- Erkaev, N. V., Lammer, H., Odert, P., Kislyakova, K. G., Johnstone, C. P., Güdel, M., & Khodachenko, M. L. 2016, MNRAS, 460, 1300, [ADS, 1601.00452](#)
- Fortney, J. J., Lodders, K., Marley, M. S., & Freedman, R. S. 2008, ApJ, 678, 1419, [ADS, arXiv:0710.2558](#)
- Gail, H.-P., & Sedlmayr, E. 2013, Physics and Chemistry of Circumstellar Dust Shells, [ADS](#)
- Heng, K. 2016, ApJL, 826, L16, [ADS, 1606.07218](#)
- Heng, K., Wyttenbach, A., Lavie, B., Sing, D. K., Ehrenreich, D., & Lovis, C. 2015, ApJL, 803, L9, [ADS, 1503.05582](#)
- Hubeny, I., Burrows, A., & Sudarsky, D. 2003, ApJ, 594, 1011, [ADS, arXiv:astro-ph/0305349](#)
- Hunter, J. D. 2007, Computing In Science & Engineering, 9, 90
- Jones, E., Oliphant, T., Peterson, P., et al. 2001, SciPy: Open source scientific tools for Python
- Knutson, H. A., Benneke, B., Deming, D., & Homeier, D. 2014, Nature, 505, 66, [ADS, 1401.3350](#)
- Koskinen, T. T., Harris, M. J., Yelle, R. V., & Lavvas, P. 2013, Icarus, 226, 1678, [ADS, 1210.1536](#)
- Kreidberg, L. et al. 2014a, Nature, 505, 69, [ADS, 1401.0022](#)
- Kreidberg, L. et al. 2014b, ApJL, 793, L27, [ADS, 1410.2255](#)
- Lecavelier Des Etangs, A., Pont, F., Vidal-Madjar, A., & Sing, D. 2008, A&A, 481, L83, [ADS, 0802.3228](#)
- Lendl, M. et al. 2012, A&A, 544, A72, [ADS, 1205.2757](#)
- Lendl, M. et al. 2016, A&A, 587, A67, [ADS, 1512.06698](#)
- Lodders, K. 2003, ApJ, 591, 1220, [ADS](#)
- Louden, T., & Wheatley, P. J. 2015, ApJL, 814, L24, [ADS, 1511.03689](#)
- Malik, M. et al. 2017, AJ, 153, 56, [ADS, 1606.05474](#)
- Mandell, A. M., Haynes, K., Sinukoff, E., Madhusudhan, N., Burrows, A., & Deming, D. 2013, ApJ, 779, 128, [ADS, 1310.2949](#)
- Morley, C. V., Fortney, J. J., Marley, M. S., Visscher, C., Saumon, D., & Leggett, S. K. 2012, ApJ, 756, 172, [ADS, 1206.4313](#)
- Morley, C. V., Fortney, J. J., Marley, M. S., Zahnle, K., Line, M., Kempton, E., Lewis, N., & Cahoy, K. 2015, ApJ, 815, 110, [ADS, 1511.01492](#)

- Parmentier, V., Fortney, J. J., Showman, A. P., Morley, C., & Marley, M. S. 2016, *ApJ*, 828, 22, [ADS, 1602.03088](#)
- Pont, F., Knutson, H., Gilliland, R. L., Moutou, C., & Charbonneau, D. 2008, *MNRAS*, 385, 109, [ADS, 0712.1374](#)
- Richard, C. et al. 2012, *JQSRT*, 113, 1276, [ADS](#)
- Rothman, L. S. et al. 2013, *JQSRT*, 130, 4, [ADS](#)
- Rothman, L. S. et al. 2010, *JQSRT*, 111, 2139, [ADS](#)
- Sanz-Forcada, J., Micela, G., Ribas, I., Pollock, A. M. T., Eiroa, C., Velasco, A., Solano, E., & Garcia-Álvarez, D. 2011, *A&A*, 532, A6, [ADS, 1105.0550](#)
- Sing, D. K. et al. 2016, *Nature*, 529, 59, [ADS, 1512.04341](#)
- Spiegel, D. S., Silverio, K., & Burrows, A. 2009, *ApJ*, 699, 1487, [ADS, 0902.3995](#)
- Stevenson, K. B. 2016, *ApJL*, 817, L16, [ADS, 1601.03492](#)
- van der Walt, S., Colbert, S. C., & Varoquaux, G. 2011, *Computing in Science & Engineering*, 13, 22
- Visscher, C., Lodders, K., & Fegley, Jr., B. 2006, *ApJ*, 648, 1181, [ADS, astro-ph/0511136](#)
- Visscher, C., Lodders, K., & Fegley, Jr., B. 2010, *ApJ*, 716, 1060, [ADS, 1001.3639](#)
- Wakeford, H. R., & Sing, D. K. 2015, *A&A*, 573, A122, [ADS, 1409.7594](#)
- Wright, N. J., Drake, J. J., Mamajek, E. E., & Henry, G. W. 2011, *ApJ*, 743, 48, [ADS, 1109.4634](#)
- Wytenbach, A. et al. 2017, *A&A*, 602, A36, [ADS, 1702.00448](#)